Chemical Engineering Journal 520 (2025) 166397

Contents lists available at ScienceDirect

Chemical Engineering Journal

journal homepage: www.elsevier.com/locate/cej

N-heterocyclic carbene as a potent $LiNO_3$-solubilizer, Li^+-solvation regulator and solid-electrolyte interphase enhancer for highly durable Lithium metal batteries

Yaoda Wang, Junchuan Liang, Xinmei Song, Tianyu Shen, Xingkai Ma, Zuoxiu Tie, Zhong Jin *

State Key Laboratory of Coordination Chemistry, MOE Key Laboratory of Mesoscopic Chemistry, MOE Key Laboratory of High Performance Polymer Materials and Technology, Jiangsu Key Laboratory of Advanced Organic Materials, Suzhou Key Laboratory of Green Intelligent Manufacturing of New Energy Materials and Devices, Tianchang New Materials and Energy Technology Research Center, Institute of Green Chemistry and Engineering, School of Chemistry and Chemical Engineering, Nanjing University, Nanjing, Jiangsu 210023, PR China

ARTICLE INFO

Keywords:
Lithium metal batteries
N-heterocyclic carbene
Lithium nitrate
Li^+ solvation shell
Solid electrolyte interphase
Synergistic-dual-additive strategy

ABSTRACT

Lithium metal batteries are considered promising high-energy-density power sources, but their development is hindered by severe Li dendrite growth and unstable solid electrolyte interphase (SEI) formation. Herein, we report the design of a synergistic-dual-additive electrolyte with unique solvation chemistry by simultaneously introducing N-heterocyclic carbene adduct with boron trifluoride (NHCABT) and lithium nitrate ($LiNO_3$) into carbonate-based electrolytes. The addition of NHCABT with electron-deficient atoms can greatly enhance the solubility of $LiNO_3$ in carbonate-based electrolytes, while the dissolution of $LiNO_3$ is highly conducive to activating boron trifluoride receptor ($-BF_3$) in the adduct. The synergistic effect of NHCABT and $LiNO_3$ markedly optimizes the Li^+ solvation sheath, induces the formation of stable SEI rich in numerous inorganic species, and effectively enhancing Li^+ conductivity. Consequently, the Li||$LiFePO_4$ batteries based on the synergistic-dual-additive electrolyte exhibit an ultralong cycling lifespan of 3000 cycles at 2.0 C and impressive low-temperature electrochemical performances at −20 °C. When paired with aggressive $LiNi_{0.8}Co_{0.1}Mn_{0.1}O_2$ (NCM811) cathodes, the synergistic-dual-additive electrolyte enables Li||NCM811 batteries to work stably for over 1000 cycles at 1.0 C. This work presents an efficient synergistic-dual-additive strategy to boost the compatibility of carbonate-based electrolytes with lithium metal anodes, providing a promising solution for constructing highly durable lithium metal batteries.

1. Introduction

Since the commercialization of lithium ion batteries (LIBs) in 1991, graphite have dominated the selection of anode materials [1,2], but its inherent theoretical specific capacity limitation cannot meet the requirements of high-energy-density energy storage [3,4]. Lithium metal anode is considered as the "holy grail" due to its ultrahigh theoretical capacity (3860 mAh g^{-1} or 2061 mAh cm^{-3}) and ultralow redox electrochemical potential (−3.04 V vs. standard hydrogen electrode, SHE) [5,6]. With the in-depth studies of Li—S and Li-air batteries, the superiorities of lithium metal anodes in boosting energy density are further highlighted [7,8]. Regardless, significant obstacles pertaining to lithium metal anodes persist and require urgent resolution, encompassing issues like the undesired side reactions with conventional organic electrolytes [5,9], the formation of a fragile solid electrolyte interface (SEI) [10–12], the uncontrollable growth of Li dendrites [13,14], and the proliferation of dead Li that posing grave safety concerns [15–17]. Substantial efforts have been devoted to tackle the aforementioned knotty problems, including interface engineering [18,19], electrolyte optimization [20,21], substrate modification [22,23], separator functionalization [24] and the employment of solid-state electrolytes [25,26].

Introducing functional electrolyte additives is demonstrated to a promising way to stabilize lithium metal anodes by tailoring the electrolyte solvation shell and optimizing the composition and structure of SEI [27–33]. Particularly, lithium nitrate ($LiNO_3$) is regarded as an effective electrolyte additive capable of regulating Li plating/stripping

* Corresponding author.
E-mail address: zhongjin@nju.edu.cn (Z. Jin).

https://doi.org/10.1016/j.cej.2025.166397
Received 25 April 2025; Received in revised form 15 July 2025; Accepted 23 July 2025
Available online 24 July 2025
1385-8947/© 2025 Elsevier B.V. All rights are reserved, including those for text and data mining, AI training, and similar technologies.

behaviors and prolonging cycling lifespan. However, the solubility of $LiNO_3$ in carbonate-based electrolytes is very poor (~800 ppm) [29,34]. Recently, various solubilizers have been proposed to enhance the solubility of $LiNO_3$ [29,30,34–36]. However, most of existing solubilizers have negligible effect on improving battery performances except for contributing to the dissolution of $LiNO_3$, and are even likely to deteriorate the battery stability to some extent [30]. Therefore, it is highly desirable to develop multifunctional solubilizers that can effectively enhance the solubility of $LiNO_3$ while simultaneously further improving the overall performance of batteries.

Herein, an advanced synergistic-dual-additive electrolyte is developed by simultaneously introducing N-heterocyclic carbene adduct with boron trifluoride (NHCABT) and $LiNO_3$ into conventional carbonate-based electrolytes. The added NHCABT can significantly improve the solubility of $LiNO_3$ from 0.08 wt% (0.0145 M) to 1.0 wt% (0.181 M), and enable NO_3^- to fully participate in the Li^+ solvation sheath (Fig. 1a),

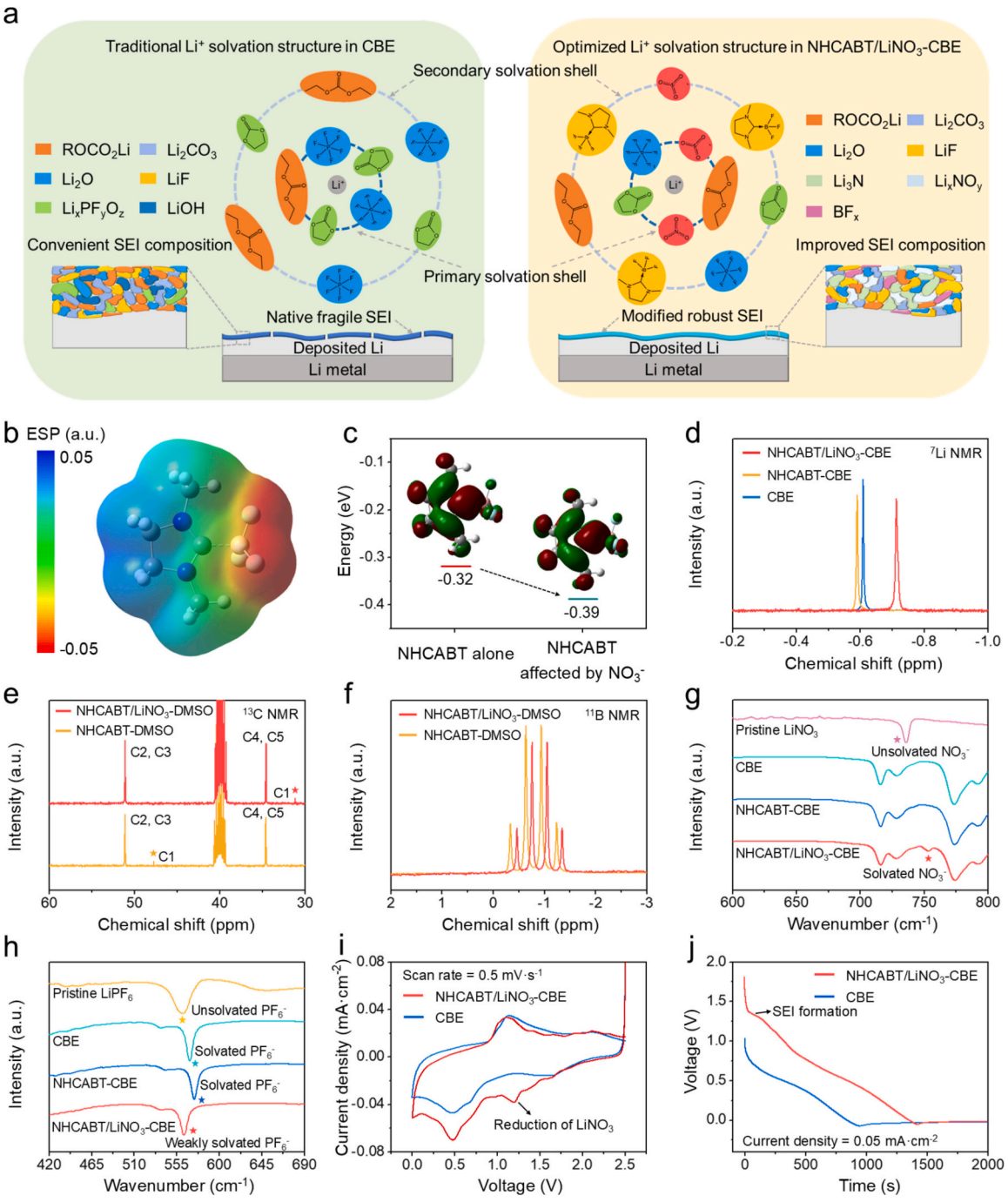

Fig. 1. Synergistic effect of NHCABT/$LiNO_3$-CBE on the regulation of Li^+ solvation structure and the formation of additive-modified SEI. (a) Schematic illustration comparing the Li^+ solvation structures and the SEI compositions in conventional CBE and NHCABT/$LiNO_3$-CBE. (b) Simulated ESP mapping of NHCABT. (c) LUMO energy levels of NHCABT alone and NHCABT affected by NO_3^-. (d) ^{7}Li NMR spectra of conventional CBE, NHCABT-CBE and NHCABT/$LiNO_3$-CBE. (e) ^{13}C and (f) ^{11}B NMR spectra of NHCABT-DMSO and NHCABT/$LiNO_3$-DMSO. (g) ATR-FTIR spectra of pristine $LiNO_3$ powder, conventional CBE, NHCABT-CBE and NHCABT/$LiNO_3$-CBE. (h) ATR-FTIR spectra of pristine $LiPF_6$ powder, conventional CBE, NHCABT-CBE and NHCABT/$LiNO_3$-CBE. (i) CV curves of Li||Cu half batteries based on conventional CBE and NHCABT/$LiNO_3$-CBE at a scan rate of 0.5 mV s^{-1} from 0 to 2.5 V. (j) Galvanostatic voltage profiles of Li deposition on Cu substrate in conventional CBE and NHCABT/$LiNO_3$-CBE at a current density of 0.05 mA cm^{-2}.

while the dissolved $LiNO_3$ can in turn activate boron trifluoride receptors (–BF_3) of NHCABT, markedly improving its reactivity with lithium metal. Benefiting from the efficient participation and synergistic effect of NHCABT and $LiNO_3$, an optimized Li^+ solvation structure is achieved, which induces the formation of a uniform and stable SEI rich in Li_xN_y, Li_xNO_y, LiF and BF_x species (Fig. 1a), and efficiently inhibits the decomposition of PF_6^- to release harmful HF. Moreover, the NHCABT/$LiNO_3$-modified electrolyte exhibits the increased ionic conductivities, boosting the improved low-temperature electrochemical properties of batteries. Consequently, the Li||Li symmetric batteries based on the NHCABT/$LiNO_3$-modified electrolyte display stable Li plating/stripping behaviors for over 1000 h with an ultralow overpotential of 40 mV at 1.0 mA cm^{-2}. The modified Li||$LiFePO_4$ (LFP) batteries exhibit outstanding cycling stability for over 3000 cycles and impressive rate performance at 15.0 C. Furthermore, the modified Li||LFP batteries assembled with high-loading LFP cathodes (~15.3 mg cm^{-2} or ~2.6 mAh cm^{-2}) can cycle stably at a low temperature of −20 °C. Likewise, the Li||$LiNi_{0.8}Co_{0.1}Mn_{0.1}O_2$ (NCM811) batteries based on NHCABT/$LiNO_3$-modified electrolyte also perform well, delivering a reversible discharge capacity of 138.3 mAh g^{-1} after 1000 cycles. This work presents novel insights into the rational regulation of solvation chemistry to optimize carbonate-based electrolytes, offering a synergistic dual-additive strategy for achieving high-stable and long-life lithium metal batteries.

2. Results and discussion

The incorporation of NHCABT additive can efficiently tailor the solvation chemistry and promote the solubility of $LiNO_3$ in carbonate-based electrolytes. Due to the electron-deficient B and C1 atoms in NHCABT (Fig. S1), the solubility of $LiNO_3$ in conventional carbonate-based electrolyte (1.0 M $LiPF_6$ in ethylene carbonate/diethyl carbonate (EC/DEC), denoted as CBE,) can be upgraded from 0.08 wt% (0.0145 M) to 1.0 wt% (0.181 M) by introducing 0.75 wt% NHCABT as a competitive solubilizer (Fig. S2 and S3 and Table S1). The preparation process of NHCABT/$LiNO_3$ synergistic-dual-additive modified carbonate-based electrolyte (denoted as NHCABT/$LiNO_3$-CBE) was detailed in the Experimental section of Supporting Information. The as-prepared NHCABT/$LiNO_3$-CBE demonstrated remarkable stability, maintaining its transparency and free from precipitations even after remaining stationary for 30 days (Fig. S4).

To deeply understand the effects of NHCABT on regulating electrolyte solvation structure, density functional theory (DFT) calculations and molecular dynamics (MD) simulations were performed systematically. Electrostatic potential (ESP) calculation demonstrated the electron deficiency of B and C1 atoms in NHCABT due to the strong electron-withdrawing property of F atoms (Fig. 1b). The charge distribution of NHCABT, analyzed using Mulliken populations, quantitatively confirmed the electro-positivity of B and C1 atoms. This electropositivity indicated the potential interactions between B and C1 atoms with NO_3^- anions, thus predicting the capacity of NHCABT to dissolve $LiNO_3$ (Fig. S5a). The interaction between NHCABT and NO_3^- was more intuitively reflected by the optimized geometry of NHCABT-NO_3^-. The differential charge density distribution of NHCABT-NO_3^- indicated a marked interaction between B and C1 atoms of NHCABT and O atoms of NO_3^- (Fig. S6). The charge distribution of NHCABT-NO_3^- simulated by the Mulliken populations also revealed significant differences in atomic charge, demonstrating an evident interaction between NHCABT and NO_3^- (Fig. S7a), which was further verified by the ESP mapping of NHCABT-NO_3^- (Fig. S7b). Moreover, compared with the NHCABT alone, the lowest unoccupied molecular orbital (LUMO) energy level of NHCABT affected by NO_3^- markedly decreased (Fig. 1c), which theoretically illustrated that the dissolved $LiNO_3$ could in turn activate the boron trifluoride receptors (–BF_3) in NHCABT and promote the reaction of –BF_3 with metallic lithium to form LiF and BF_x components in the SEI. The LUMO energy level change of NO_3^- was also investigated by DFT calculation (Fig. S8). Although the LUMO energy level of NO_3^- affected by NHCABT showed a slight increase, it still remained much lower than those of solvent molecules and NHCABT in the electrolyte, implying superior film-forming ability of NO_3^- and the existence of synergistic interaction between the NHCABT and NO_3^-. MD simulations were performed to clarify the changes of Li^+ solvation structures in different electrolyte systems (Fig. S9). For the single-additive electrolyte system (NHCABT-CBE), the Li^+-F(NHCABT) peak was observed at the distance of 3.43 Å, which was greater than those of Li^+-(O)EC and Li^+-(O)DEC, and Li^+-F(PF_6^-). Combined with the simulation results of coordination numbers, it was concluded that NHCABT molecules in NHCABT-CBE primarily populated the Li^+ second solvation shell and showed negligible direct coordination with Li^+ ions. After further adding $LiNO_3$ into the NHCABT-CBE, a marked Li^+-O(NO_3^-) peak was observed at the distance of 1.75 Å, demonstrating the close interaction of NO_3^- anions with Li^+ ions and the involvement of NO_3^- in Li^+ solvation shell. Moreover, compared with the simulation results of conventional CBE and NHCABT-CBE, the NHCABT/$LiNO_3$-CBE demonstrated the reduced coordination numbers of Li^+-(O)EC and Li^+-(O)DEC, indicating that the number of solvent molecules involved in Li^+ solvation structure had decreased, which was conducive to improving the desolvation kinetics.

Nuclear magnetic resonance (NMR) analyses were conducted to clearly reveal the solubilization mechanism of $LiNO_3$ by NHCABT additive. Upon introducing NHCABT into CBE, the ^7Li NMR signal shifted from −0.61 to −0.59 ppm (Fig. 1d), demonstrating a deshielding effect brought from electron-deficient B and C1 atoms of NHCABT [36]. Nevertheless, the peak of ^7Li signal moved inversely to −0.71 ppm after the simultaneous addition of NHCABT and $LiNO_3$, indicating the participation of electron-donating NO_3^- in Li^+ solvation structure. The interaction and synergism between NHCABT and $LiNO_3$ were also verified by ^{13}C and ^{11}B NMR spectra for dimethyl-d_6 sulfoxide solutions of NHCABT or NHCABT/$LiNO_3$ (denoted as NHCABT-DMSO and NHCABT/$LiNO_3$-DMSO). Different with the C2, C3, C4, and C5 signals in ^{13}C NMR spectra (Fig. 1e and S10), the C1 peak showed a strong upfield shift from 47.76 to 31.14 ppm, indicating a significant interaction between C1 and NO_3^-, which is the origin of $LiNO_3$ solubilization effect. The interaction enabled the lone pair electrons on C1 atom to further transfer to B atom (Fig. S5b), leading to the activation of –BF_3 receptors. Therefore, a clear upfield shift was also observed in ^{11}B NMR spectra (Fig. 1f), verifying the reliability of the theoretical calculation results. The activated –BF_3 receptors possessed the significantly enhanced reactivity with lithium metal, which is of great importance for the formation of a stable SEI rich in LiF and BF_x species on the lithium electrode surface.

The activation of –BF_3 receptors by the dissolution of $LiNO_3$ was visually verified by the color differences of Li foils dropped with different electrolytes. As shown in Fig. S11, only NHCABT/$LiNO_3$-CBE-soaked Li foils exhibited the color transition from bright to dark. Energy dispersive X-ray spectrometry (EDX) characterizations for the above treated Li foils also demonstrated the spontaneous reaction of activated –BF_3 receptors with lithium metal, reflected by the significantly increased content of F element (Fig. S12). To identify the reaction products of the spontaneous reaction, the above treated Li foils were further characterized by X-ray photoelectron spectroscopy (XPS) technique. The characteristic peaks corresponding to LiF and BF_x species were detected in the F 1s and B 1s spectra (Fig. S13), confirming the crucial role of activated –BF_3 receptors in optimizing SEI composition. Additionally, attenuated total reflectance-Fourier transform infrared (ATR-FTIR) spectroscopy was conducted to further probe the transition of Li^+ solvation structure. The typical characteristic peak of unsolvated NO_3^- was located at 737 cm^{-1}, while the solvated NO_3^- in NHCABT/$LiNO_3$-CBE exhibited a strong blueshift (~16 cm^{-1}) (Fig. 1g), confirming the successful introduction of NO_3^- into Li^+ solvation sheath. On the contrary, the FTIR peak at 569 cm^{-1} corresponding to the solvated PF_6^- showed a significant redshift (~6 cm^{-1}) in NHCABT/$LiNO_3$-CBE (Fig. 1h), illustrating that PF_6^- anions were partially removed from the

Li^+ solvation sheath [37]. The weakened interaction between PF_6^- and Li^+ is beneficial to suppress PF_6^- decomposition during battery operation, and thus the addition of NHCABT and $LiNO_3$ is expected to prevent harmful HF generation [35].

To evaluate the oxidation resistance of NHCABT/$LiNO_3$-CBE and gain insight into the formation mechanism of NHCABT/$LiNO_3$-modified SEI, a series of electrochemical measurements were conducted. Cyclic voltammetry (CV) was employed to detect the reduction of NO_3^- in the range of 0 to 2.5 V (Fig. 1i). In addition to the reduction peak at ~0.3 V derived from the underpotential deposition of Li [29], a broad peak between 1.3 and 1.6 V was observed in NHCABT/$LiNO_3$-CBE, representing the decomposition of $LiNO_3$. The difference of Li deposition behaviors in various electrolytes was further analyzed by a chronopotentiometry method (Fig. 1j), an additional voltage platform at

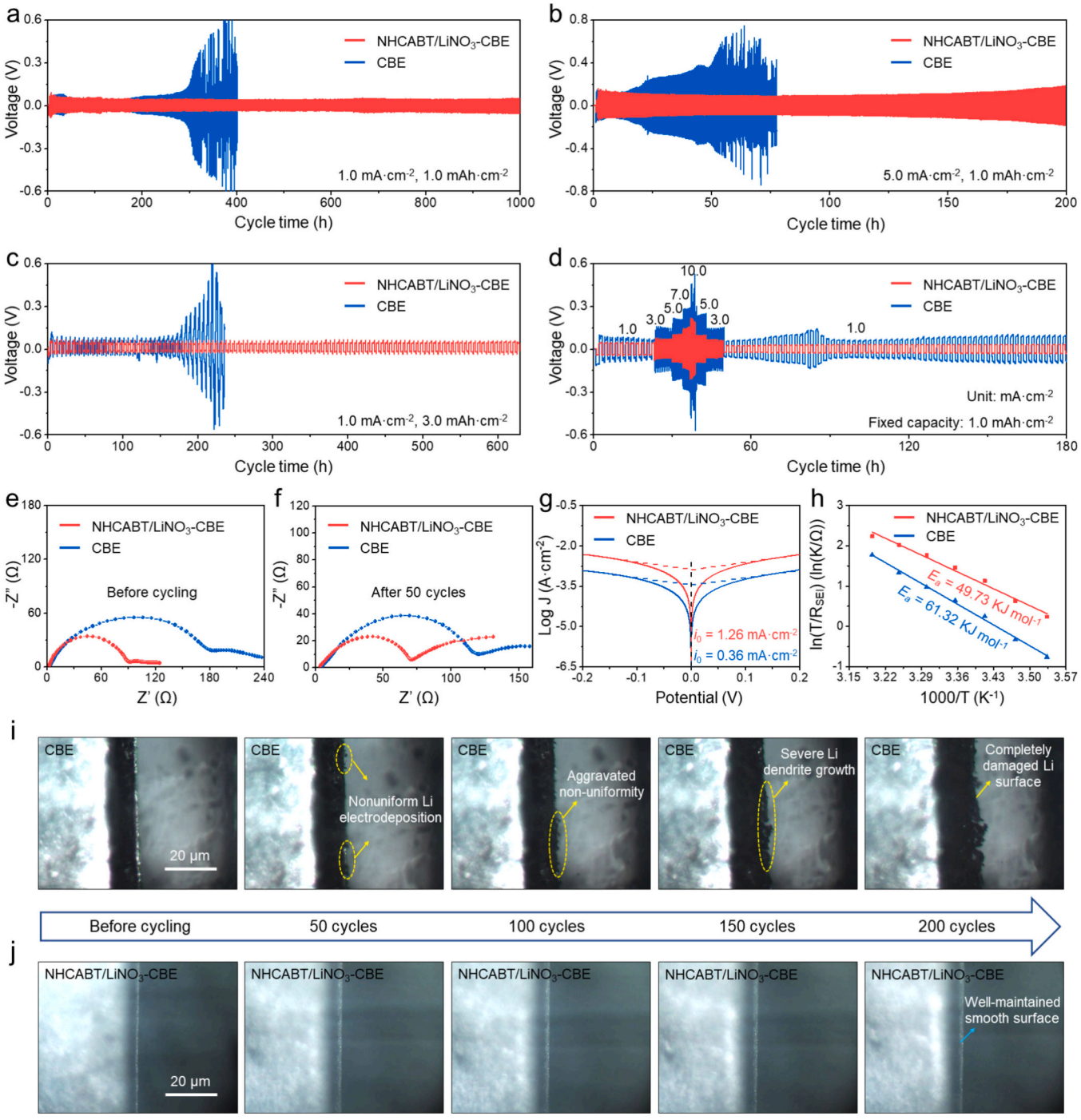

Fig. 2. Electrochemical performance comparisons of Li||Li symmetric batteries based on NHCABT/$LiNO_3$-CBE and conventional CBE. (a-c) Galvanostatic cycling stability of Li||Li symmetric batteries measured at (a) 1.0 mA cm^{-2} with a capacity of 1.0 mAh cm^{-2}, (b) 5.0 mA cm^{-2} with a capacity of 1.0 mAh cm^{-2}, and (c) 1.0 mA cm^{-2} with a capacity of 3.0 mAh cm^{-2}. (d) Rate performance of Li||Li symmetric batteries measured at different current densities from 1.0 to 10.0 mA cm^{-2} with a fixed capacity of 1.0 mAh cm^{-2}. (e, f) EIS analyses of Li||Li symmetric batteries (e) before cycling and (f) after 50 cycles. (g) Exchange current density comparison based on the Tafel curves of Li||Li symmetric batteries measured at a scan rate of 5.0 mV s^{-1} from −0.2 to 0.2 V. (h) Arrhenius behavior of the reciprocal R_{SEI} and the calculated E_a for Li^+ diffusion through SEI. (i, j) *Operando* optical microscopy observation of Li plating/stripping processes in (i) conventional CBE and (j) NHCABT/$LiNO_3$-CBE at a current density of 3.0 mA cm^{-2}.

~1.4 V was detected, suggesting the SEI formation derived from the $LiNO_3$ decomposition. The CV and chronopotentiometry results demonstrated that $LiNO_3$ could be preferentially reduced at a higher potential (~1.4 V) in NHCABT/$LiNO_3$-CBE, thus ensuring the formation of stable SEI with high Li^+ conductivity. Moreover, the oxidation resistance of NHCABT/$LiNO_3$-CBE was evaluated by measuring linear sweep voltammetry (LSV) curves of Li||carbon-coated Al foil half batteries. As displayed in Fig. S14, the LSV curves of NHCABT/$LiNO_3$-CBE exhibited a wider electrochemical stability window and a characteristic signal corresponding to the formation of a CEI layer, implying that the addition of NHCABT and $LiNO_3$ could effectively boost the oxidation resistance and suppress the electrolyte decomposition when paired with high-voltage cathodes.

To evaluate the reliability and practicability of NHCABT/$LiNO_3$-CBE, Li plating/stripping stability was investigated based on Li||Li symmetric batteries. When cycled at 1.0 mA cm^{-2} with a capacity of 1.0 mAh cm^{-2}, the batteries with conventional CBE displayed significantly increased voltage hysteresis and severe voltage fluctuations only after 300 h (Fig. 2a), mainly due to the ceaseless consumption of limited electrolytes, the uncontrolled proliferation of Li dendrites, and the formation of a fragile native SEI [38]. Comparatively, stable Li plating/stripping behavior was achieved for the batteries based on NHCABT/$LiNO_3$-CBE for more than 1000 h, with an ultralow overpotential of ~40 mV (Fig. S15). When the current density was increased to 2.0 and 3.0 mA cm^{-2} (Fig. S16a, b), stable Li plating/stripping processes in the batteries with conventional CBE could only last for 200 and 100 h, respectively, followed by dramatic voltage fluctuations until the batteries completely failed. However, the batteries with NHCABT/$LiNO_3$-CBE showed superior cycling stability for over 520 h at 2.0 mA cm^{-2} and 400 h at 3.0 mA cm^{-2} with low overpotentials of ~80 mV and ~130 mV, respectively. At a higher current density of 5.0 mA cm^{-2} (Fig. 2b), the differences in cycling performance of batteries became more obvious. The batteries with conventional CBE presented continuous increase in voltage hysteresis and finally suffered from a short circuit after 60 h. By comparison, a steady Li plating/stripping process could still be realized by the batteries with NHCABT/$LiNO_3$-CBE at such a high current density for over 200 h. Moreover, the Li plating/stripping stability at a higher capacity of 3.0 mAh cm^{-2} was also investigated (Fig. 2c). For the batteries with conventional CBE, unstable galvanostatic cycling profiles with a sharp voltage divergence of more than 450 mV emerged after merely 220 h. By comparison, the batteries with NHCABT/$LiNO_3$-CBE could cycle stably for over 630 h, and an ultralow voltage polarization of ~30 mV was well maintained throughout the cycling process. To verify the performance improvement of the NHCABT/$LiNO_3$-modified batteries under extreme charge/discharge conditions, the Li plating/stripping stability of Li||Li symmetric batteries was further tested at 10.0 mA cm^{-2} with a capacity of 10.0 mAh cm^{-2} (Fig. S16c). The batteries with NHCABT/$LiNO_3$-CBE demonstrated markedly prolonged cycling lifespans and lower overpotentials, highlighting the practical potential of NHCABT/$LiNO_3$-CBE.

The effect of additive contents on the electrochemical performances of lithium metal electrodes was further explored (Fig. S17). The Li||Li symmetric batteries with different mass ratios of NHCABT to $LiNO_3$ were cycled at 1.0 and 2.0 mA cm^{-2} with a capacity of 1.0 mAh cm^{-2}. As a result, the batteries with 0.75 wt% NHCABT/1.0 wt% $LiNO_3$-CBE exhibited the best cycling stability compared with the others. Moreover, the Li||Li symmetric batteries based on 0.75 wt% NHCABT/1.0 wt% $LiNO_3$-CBE also exhibited better cycling performance compared to the control groups with higher $LiNO_3$ concentrations (over 1.0 wt%) (Fig. S18), indicating that a higher concentration of $LiNO_3$ in conventional CBEs was not necessarily better. Therefore, the electrolyte formula of 0.75 wt% NHCABT/1.0 wt% $LiNO_3$-CBE was adopted for the subsequent electrochemical measurements and characterizations. The influence of NHCABT as a single additive on battery performance was also investigated (Fig. S19). The results showed that the improvement of single NHCABT additive on Li plating/stripping stability was very limited, illustrating that the $–BF_3$ receptors alone could not effectively enhance the cycling stability of lithium metal electrodes, which was mainly due to the fact that the $–BF_3$ receptors were not activated in the absence of $LiNO_3$. To deeply understand the effect of activated $–BF_3$ receptors on Li plating/stripping stability, we directly introduced a single $LiBF_4$ additive into CBE (denoted as $LiBF_4$-CBE) to simulate activated $–BF_3$ receptors with BF_4^- anions and investigate the cycling stability of lithium metal electrodes paired with $LiBF_4$-CBE at various current densities and capacities. Compared with conventional CBE, the batteries based on the $LiBF_4$-CBE demonstrated the prolonged cycling lifespans and decreased overpotentials (Fig. S20), indicating that BF_4^- anions (similar to the activated $–BF_3$ receptors) could effectively improve the electrolyte compatibility with lithium metal electrodes and enable the formation of a stable SEI. Therefore, it was concluded that the activated $–BF_3$ receptors played a prominent role in achieving stable Li plating/stripping behaviors of lithium metal electrodes. To further highlight the superiority of NHCABT/$LiNO_3$-CBE, the cycling performance of Li||Li symmetric batteries with ether-based electrolyte (1.0 M LiTFSI in dioxolane/dimethoxyethane (DOL/DME) with 1.0 wt% $LiNO_3$, denoted as EBE) was also tested at different current densities and capacities (Fig. S21). The results verified that more stable Li plating/stripping processes were achieved in NHCABT/$LiNO_3$-CBE compared to that in EBE, indicating that NHCABT and $LiNO_3$ as synergistic dual additives could effectively improve the compatibility of CBE with lithium metal electrodes, induce the formation of stable and highly Li^+ conducting SEI, and suppress the proliferation of Li dendrites, thereby boosting the cycling performance of lithium metal electrodes in CBE to a higher level than that in EBE.

The rate performance of Li||Li symmetric batteries with different electrolytes was evaluated at various current densities from 1.0 to 10.0 mA cm^{-2} with a fixed capacity of 1.0 mAh cm^{-2} (Fig. 2d). With the increase of current density, the batteries with conventional CBE exhibited sharply increased voltage hysteresis and irregular voltage curves at 10 mA cm^{-2}, indicating the batteries based on conventional CBE could hardly work under such a high current density [39]. In contrast, the batteries with NHCABT/$LiNO_3$-CBE exhibited flat voltage platforms with desired regularity and low overpotentials of 43, 65, 82, 120 and 178 mV at 1.0, 3.0, 5.0, 7.0 and 10.0 mA cm^{-2}, respectively (Fig. S22). The cycling stability and rate performance tests fully revealed that the NHCABT/$LiNO_3$-CBE could efficiently induce the formation of a uniform and stable SEI with high Li^+ conductivity, thereby resulting in the decreased voltage polarization and the suppressed Li dendrite growth. To verify the accelerated charge transfer kinetics in NHCABT/$LiNO_3$-CBE, electrochemical impedance spectroscopy (EIS) measurements based on Li||Li symmetric batteries were conducted. Before cycling (Fig. 2e), the interfacial resistance of the batteries with conventional CBE was 176.3 Ω, much higher than that of the batteries with NHCABT/$LiNO_3$-CBE (86.9 Ω). After 50 cycles (Fig. 2f), a lower interfacial resistance (67.3 Ω) for the batteries with NHCABT/$LiNO_3$-CBE was obtained, while the batteries with CBE still maintained a high interfacial resistance of 115.9 Ω. The above results illustrated that the NHCABT/$LiNO_3$-CBE achieved faster Li^+ transport at the electrode/electrolyte interfaces, benefiting from the formation of highly Li^+ conducting SEI and the well-regulated Li^+ solvation structure. Exchange current densities (i_0) calculated according to the Tafel plots of Li||Li symmetric batteries were also compared (Fig. 2g). The batteries with NHCABT/$LiNO_3$-CBE exhibited a considerable i_0 value of 1.259 mA·cm^{-2}, much higher than that of the batteries with conventional CBE (0.358 mA·cm^{-2}), further confirming the superior Li plating/stripping kinetics in NHCABT/$LiNO_3$-CBE. Additionally, apparent activation energy (E_a) for Li^+ diffusion through SEI was calculated via measuring temperature-dependent R_{SEI} values (Fig. S23). By linearly fitting $\ln(T/R_{SEI})$ versus $1/T$ (Fig. 2h) [40], the E_a value was demonstrated to decrease from 61.32 kJ mol^{-1} in conventional CBE to 49.73 kJ mol^{-1} in NHCABT/$LiNO_3$-CBE, which strongly confirmed that the formed stable SEI supported rapid Li^+ migration.

To intuitively reveal the morphology evolution of lithium metal electrodes during the cycling processes and corroborate the effectiveness of NHCABT/$LiNO_3$-derived SEI in the suppression of Li dendrite growth, an optical microscope was employed to in-situ monitor Li plating/stripping behaviors at the electrolyte/electrode interfaces (Fig. 2i, j). Before cycling, the pristine lithium metal electrodes displayed a smooth and flat surface morphology in both electrolytes. After 50 cycles, a few visible and mossy-like Li protrusions were observed for the lithium metal electrodes in conventional CBE. With the proceeding of Li plating/stripping cycles, these protrusions nucleated and aggregated to form numerous Li dendrites, and completely covered the lithium electrode surface after 200 cycles. In sharp contrast, the lithium electrodes in NHCABT/$LiNO_3$-CBE well maintained steady Li plating/stripping behaviors, presenting uniform and dense surface morphology without any visible mossy-like Li dendrites during the whole cycling process. This fully demonstrates that NHCABT and $LiNO_3$ as synergistic dual additives could effectively promote uniform Li electrodeposition and markedly inhibit Li dendrite growth, thus leading to greatly improved electrochemical kinetics and excellent cycling stability.

To gain further insight into the modulation effects of additives, the surface morphologies and compositions of cycled lithium metal electrodes retrieved from the Li||Li symmetric batteries with different electrolytes were characterized and investigated. EDX analysis and corresponding elemental mappings of the cycled lithium metal electrodes in NHCABT/$LiNO_3$-CBE exhibited uniform distribution of B, C, N, O, F and P elements (Fig. S24), confirming the efficient participation of NHCABT and $LiNO_3$ in the SEI formation. Scanning electron microscope (SEM) characterization clearly presented the huge differences in surface morphology and microstructure of lithium metal electrodes after cycling in different electrolytes. When using conventional CBE, the cycled lithium electrodes displayed a loose and rough surface with conspicuous cracks (Fig. 3a). Further magnified SEM images (Fig. 3b, c) showed that the porous lithium metal surface was completely covered by mossy-like Li dendrites, indicating the poor compatibility of conventional CBE with lithium metal electrodes. Moreover, the cross-section SEM image showed that the substrate of lithium electrodes was severely corroded by conventional CBE (Fig. 3d), presenting a rough and loose microstructure. In contrast, prominent preservation of surface morphology was observed for the lithium electrodes in NHCABT/$LiNO_3$-CBE, showing a smooth surface morphology without any visible microcracks and Li dendrites (Fig. 3e-g) and an even microstructure from the side view (Fig. 3h). These results prove that the synergistic dual additives are able to promote the formation of a protective SEI and regulate Li^+ solvation chemistry, resulting in a uniform and dendrite-free Li electroplating morphology. Atomic force microscopy (AFM) was also employed to investigate the surface flatness of the cycled Li metal electrodes

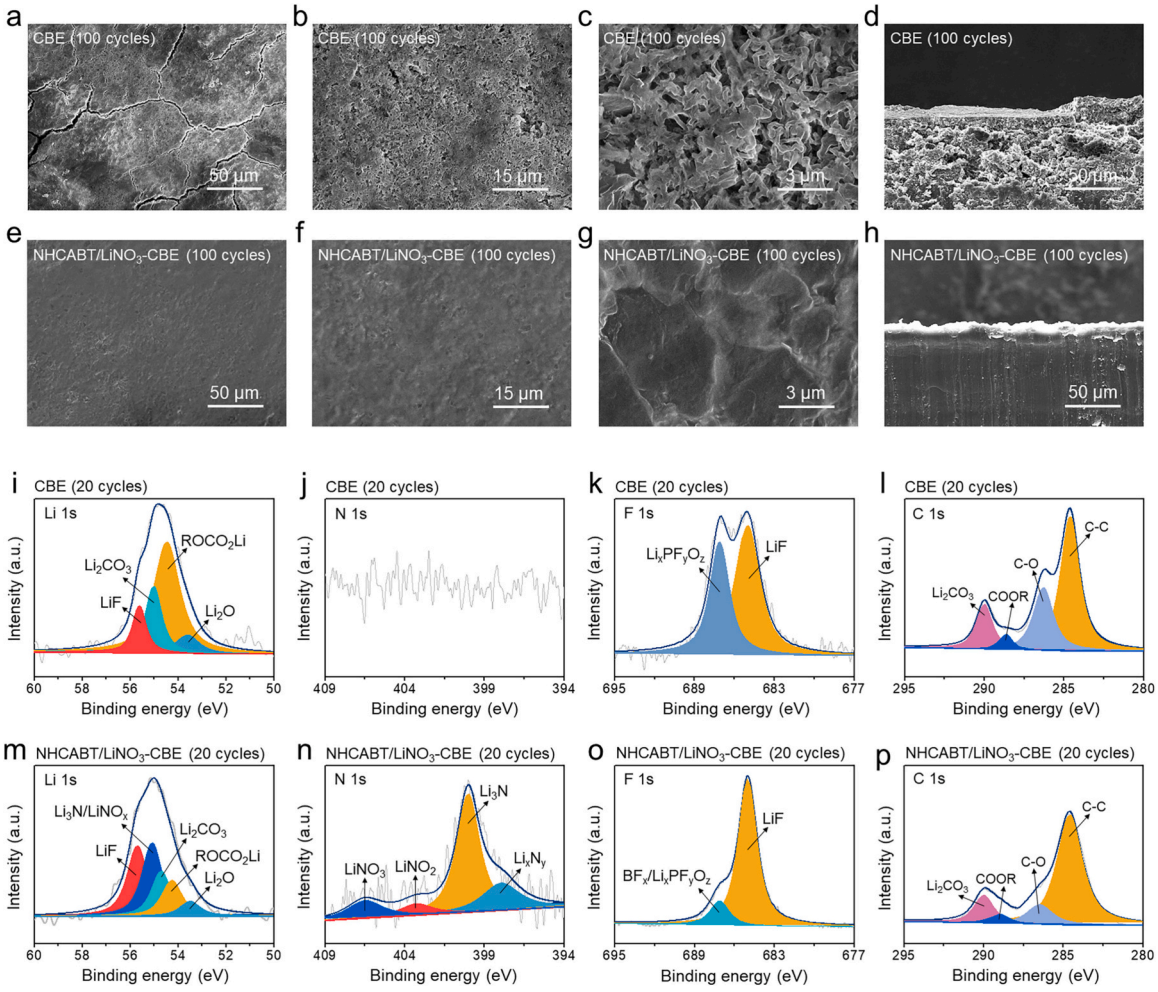

Fig. 3. Surface morphology and composition characterizations of cycled lithium metal electrodes in NHCABT/$LiNO_3$-CBE and conventional CBE. (a-c) Top-view and (d) cross-section SEM images of cycled lithium metal electrodes retrieved from Li||Li symmetric batteries with conventional CBE after 100 cycles. (e-g) Top-view and (h) cross-section SEM images of cycled lithium electrodes retrieved from Li||Li symmetric batteries with NHCABT/$LiNO_3$-CBE after 100 cycles. (i-l) High-resolution XPS spectra at (i) Li 1s, (j) N 1s, (k) F 1s, and (l) C 1s regions of cycled lithium metal electrodes retrieved from Li||Li symmetric batteries with conventional CBE after 20 cycles. (m-p) High-resolution XPS spectra at (m) Li 1s, (n) N 1s, (o) F 1s, and (p) C 1s regions of cycled lithium metal electrodes retrieved from Li||Li symmetric batteries with NHCABT/$LiNO_3$-CBE after 20 cycles.

(Fig. S25). The Li metal electrodes cycled in conventional CBE displayed a rough and uneven topography with distinct surface undulations, indicating the occurrence of severe dendritic Li proliferation. In contrast, the AFM topography of Li metal electrodes cycled in NHCABT/$LiNO_3$-CBE demonstrated improved surface smoothness, illustrating that the NHCABT/$LiNO_3$-CBE could efficiently facilitate homogeneous Li deposition and suppress Li dendrite growth, which was mainly benefited from the formation of a stable inorganic-rich SEI and its superior ion-transport ability.

XPS characterization was conducted to identify the surface compositions of cycled lithium metal electrodes in different electrolytes. When using conventional CBE, four typical peaks of LiF, Li_2CO_3, $ROCO_2Li$ and Li_2O species were detected from the Li 1s spectra at 55.7, 54.8, 54.4 and 53.6 eV, respectively (Fig. 3i). By comparison, an additional peak assigned to Li_3N and/or $LiNO_x$ is observed at 55.2 eV for NHCABT/$LiNO_3$-CBE (Fig. 3m), indicating that the introduction of NO_3^- anions induced the formation of Li_3N and $LiNO_x$ components [29,41], which were conducive to enhancing the ionic conductivity and electrochemical stability of SEI [42,43]. The N 1s spectrum of cycled lithium electrodes in conventional CBE revealed an absence of nitrogenous species (Fig. 3j), while the SEI formed in NHCABT/$LiNO_3$-CBE displayed four peaks at 406.5, 403.3, 400.0 and 397.9 eV, corresponding to $LiNO_3$, $LiNO_2$, Li_3N and Li_xN_y, respectively (Fig. 3n) [36,44]. As for F 1s spectra, two distinct peaks at 687.0 and 685.0 eV were detected when using conventional CBE (Fig. 3k), which could be assigned to $Li_xPF_yO_z$ and LiF, respectively [35]. The strong signal of $Li_xPF_yO_z$ species illustrated that PF_6^- anions participated the Li^+ solvation sheath and undergone inevitable reduction decomposition during battery operation. In contrast, the signal peak intensity corresponding to $Li_xPF_yO_z$ species was significantly weakened for the lithium electrodes cycled in NHCABT/$LiNO_3$-CBE (Fig. 3o) [45], which indicated that PF_6^- anions were removed from Li^+ solvation structure, and the LiF component in SEI mainly originated from the reaction between the activated $-BF_3$ receptors and lithium metal. The B 1s spectrum of the SEI obtained by conventional CBE show no signal (Fig. S26a), while the SEI formed in NHCABT/$LiNO_3$-CBE presented an obvious signal peak at 193.7 eV corresponding to BF_x, proving the vital role of the activated $-BF_3$ receptors in optimizing the compositions of SEI (Fig. S26c). Regarding the C 1s spectra (Fig. 3l, p), four typical peaks of Li_2CO_3, COOR, C—O and C—C were detected from the lithium electrodes cycled in both electrolytes. However, the peak intensities corresponding to COOR and C—O species decreased obviously when using NHCABT/$LiNO_3$-CBE, demonstrating the efficiently suppressed

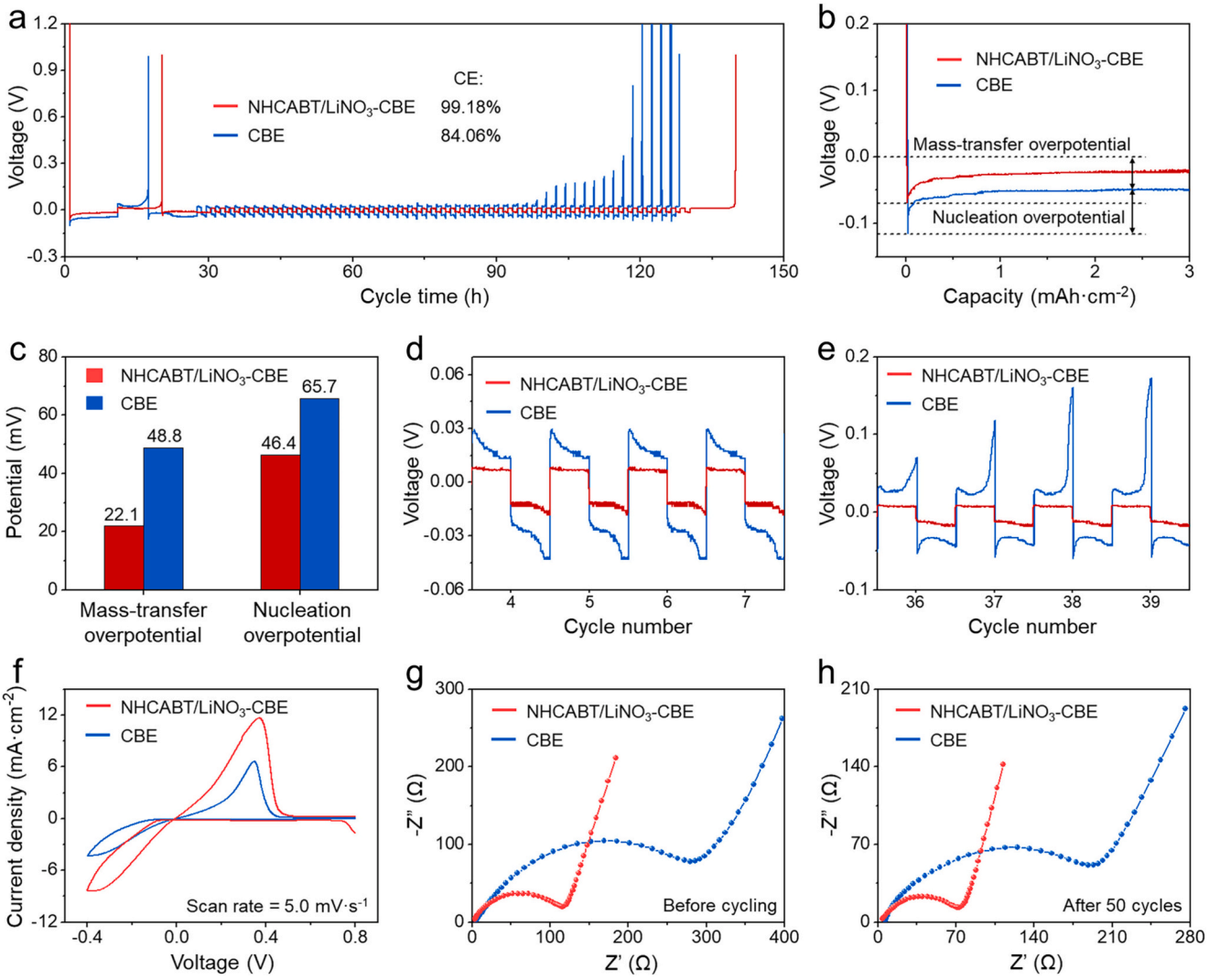

Fig. 4. Electrochemical performances of Li||Cu half batteries based on NHCABT/$LiNO_3$-CBE and conventional CBE. (a) Voltage-time curves of Li||Cu batteries measured at 0.5 mA cm^{-2} for calculating the average Coulombic efficiencies. (b) Initial Li plating profiles of Li||Cu batteries measured at 0.5 mA cm^{-2}. (c) Calculated mass-transfer overpotentials and nucleation overpotentials obtained from (b). (d, e) Detailed voltage curves at different cycles of the Li||Cu half batteries measured at 0.5 mA cm^{-2}. (f) CV curves of Li||Cu half batteries measured at a scan rate of 5.0 mV s^{-1} from −0.4 to 0.8 V. (g, h) EIS analyses of Li||Cu half batteries (g) before and (h) after 50 cycles.

decomposition of carbonate solvents. A similar conclusion was also drawn from the O 1s spectra (Fig. S26b, d). Compared to the O 1s spectrum obtained by conventional CBE, the peak intensity of Li_2O species formed in NHCABT/$LiNO_3$-CBE was markedly stronger, illustrating the presence of more inorganic components that can greatly improve the mechanical and chemical stability of SEI [32]. To investigate the gradient distribution of inorganic components in the formed SEI, *in-depth* XPS analyses for the Li metal electrodes cycled in NHCABT/$LiNO_3$-CBE were conducted after Ar^+ sputtering for 3 min (Fig. S27). The test results demonstrated that the NHCABT/$LiNO_3$-derived SEI exhibited no obvious differences in chemical compositions and relative contents of constituent species between the surface and bulk regions. The detected inorganic species, such as Li_xN_y, Li_xNO_y, LiF and BF_x, were scattered throughout the bulk phase of SEI, rather than being confined solely to the surface. Therefore, it was concluded that the NHCABT/$LiNO_3$-derived SEI possessed uniform chemical compositions and high electrochemical stability, ensuring the sustained protection for lithium metal anodes during long-term cycling processes.

To testify the effect of NHCABT/$LiNO_3$-CBE on boosting Li plating/stripping reversibility and improving nucleation and mass-transfer kinetics, the Li||Cu half batteries with different electrolytes were assembled. The average Coulombic efficiency during 50 cycles was measured firstly (Fig. 4a) [46]. For the batteries with NHCABT/$LiNO_3$-CBE, the average Coulombic efficiency was as high as 99.18 %. In comparison, the batteries with conventional CBE only delivered an unsatisfactory average Coulombic efficiency of 84.06 %. Based on the initial Li plating profiles of Li||Cu batteries, mass-transfer overpotentials and nucleation overpotentials were calculated (Fig. 4b). The mass-transfer overpotential and nucleation overpotential of lithium electrodes in conventional CBE reached 48.8 and 65.7 mV, respectively (Fig. 4c), much

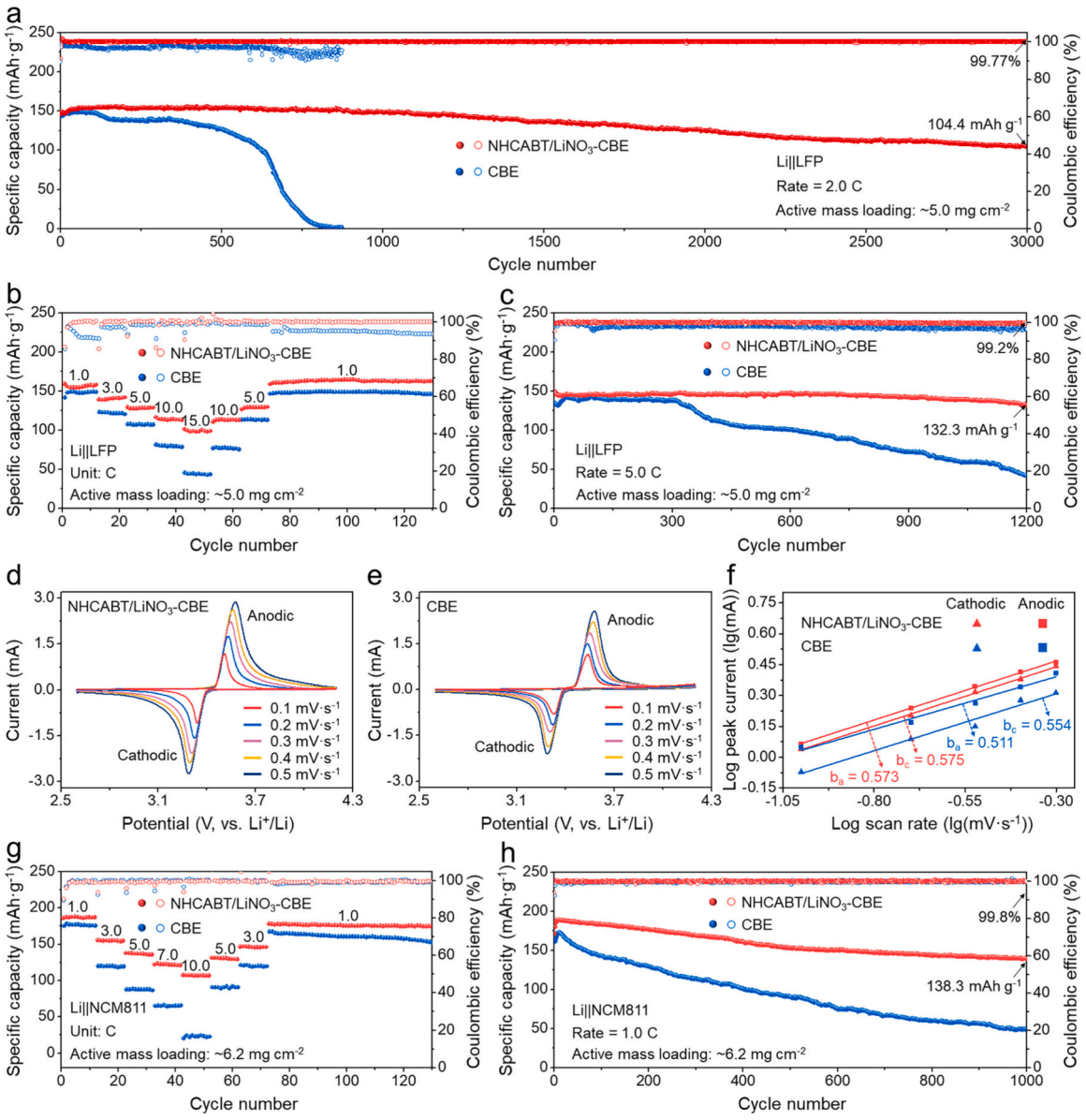

Fig. 5. Electrochemical performances of Li||LFP and Li||NCM811 batteries based on NHCABT/$LiNO_3$-CBE and conventional CBE. (a) Cycling performance of Li||LFP batteries measured at 2.0 C (1.0 C = 170 mA g^{-1}). (b) Rate performance of Li||LFP batteries measured at various current rates from 1.0 C to 15.0 C. (c) Cycling performance of Li||LFP batteries measured at 5.0 C. (d, e) CV curves of Li||LFP batteries based on (d) NHCABT/$LiNO_3$-CBE and (e) conventional CBE measured at various scan rates from 0.1 to 0.5 mV s^{-1}. (f) Comparison of the *b* values for the cathodic (b_c) and anodic (b_a) peaks. The *b*-value determination was based on the logarithmic peak currents versus scan rates. (g) Rate performance of Li||NCM811 batteries measured at various current rates from 1.0 C to 10.0 C. (h) Cycling performance of Li||NCM811 batteries measured at 1.0 C (1.0 C = 200 mA g^{-1}).

higher than those in NHCABT/$LiNO_3$-CBE (22.1 and 46.4 mV). These results revealed that NHCABT/$LiNO_3$-CBE was greatly conducive to accelerating Li^+ migration and reducing energy barrier of Li nucleation. By comparing the detailed voltage curves (Fig. 4d, e), it was found that the lithium metal electrodes in NHCABT/$LiNO_3$-CBE exhibited steady cycling behaviors with lower overpotentials, demonstrating its excellent mass-transfer kinetics and high compatibility with lithium metal electrodes. The Li plating/stripping reversibility during long-term cycling processes was further evaluated by Li||Cu half batteries (Fig. S28). When using NHCABT/$LiNO_3$-CBE, the batteries displayed markedly improved cycling stability, achieving a well-maintained CE of 99.05 % after 500 cycles. In comparison, limited cycling lifespans and significant CE fluctuations were observed for the batteries with CBE, highlighting the key role of NHCABT/$LiNO_3$ additive in boosting cycling stability and reversibility of lithium metal anodes. The CV measurement for Li||Cu half batteries with NHCABT/$LiNO_3$-CBE showed much higher current responses than that with conventional CBE (Fig. 4f), illustrating the better electrochemical kinetics for Li plating/stripping achieved by NHCABT/$LiNO_3$-CBE. Additionally, the Nyquist plots collected from Li||Cu half batteries before and after 50 cycles (Fig. 4g, h) revealed that the electrolyte resistances and interfacial resistances of the batteries with NHCABT/$LiNO_3$-CBE were lower than those with conventional CBE, further confirming rapider charge transfer enabled by the synergistic dual additives.

To examine the practical feasibility of NHCABT/$LiNO_3$-CBE, lithium metal batteries based on LFP and NCM811 cathodes were assembled and systematically studied. The Li||LFP batteries with conventional CBE exhibited severe capacity decay and Coulombic efficiency fluctuations, and the discharge capacity was rapidly attenuated to near zero after 800 cycles at 2.0 C (Fig. 5a). In sharp contrast, the Li||LFP batteries with NHCABT/$LiNO_3$-CBE displayed an ultralong cycling lifespan of more than 3000 cycles, maintaining a considerable specific discharge capacity of 104.4 mAh g^{-1} and an ultrahigh Coulombic efficiency of 99.77 %. The rate performance of Li||LFP batteries was investigated under different current rates from 1.0 to 15.0 C (Fig. 5b). The Li||LFP batteries with conventional CBE showed remarkable capacity decay when the current densities increased, while the batteries with NHCABT/$LiNO_3$-CBE delivered well-maintained specific discharge capacities of 155.3, 140.2, 127.7, 133.2 and 98.1 mAh g^{-1} at 1.0, 3.0, 5.0, 10.0, and 15.0 C, respectively. After the current rate returned to 1.0 C, the batteries with NHCABT/$LiNO_3$-CBE delivered a well-recovered discharge capacity of 162.7 mAh g^{-1}. In the charge/discharge profiles (Fig. S29), smaller potential differences between the charge/discharge plateaus were observed for the batteries with NHCABT/$LiNO_3$-CBE, further illustrating the lower voltage polarization and faster Li^+ transfer kinetics.

The cycling stability of Li||LFP batteries was also tested at 5.0 C to verify the practicability of NHCABT/$LiNO_3$-CBE in boosting fast charge/discharge performance (Fig. 5c). For the Li||LFP batteries with conventional CBE, an abrupt capacity degradation behavior occurred after 320 cycles, and then the specific discharge capacity decreased continuously. After 1200 cycles, the batteries were close to failure and could only deliver a reversible capacity of 41.6 mAh g^{-1}. In contrast, the Li||LFP batteries with NHCABT/$LiNO_3$-CBE exhibited markedly improved cycling stability, delivering a high remaining capacity of 132.3 mAh g^{-1} after 1200 cycles, corresponding to a remarkable capacity retention of 88.8 %. The electrochemical tests of Li||LFP batteries fully confirmed that NHCABT/$LiNO_3$-CBE could efficiently promote rapid Li^+ transport and improve Li plating/striping stability at high current rates. Notably, the extraordinary cycling stability of Li||LFP batteries using NHCABT/$LiNO_3$-CBE is highly competitive compared to most of reported Li||LFP batteries modified by other electrolyte additives (Table S2). CV measurements of Li||LFP batteries were carried out at different scan rates to examine the key role of NHCABT/$LiNO_3$-CBE in improving reaction kinetics of cathodes (Fig. 5d, e). With the increase of scan rates, the redox peaks for both electrolytes displayed increased peak currents and reaction overpotentials. By analyzing the relationship of the current changes with respect to the scan rates based on $i = a \cdot v^b$ (where i is the peak current, v is the scan rate, and a, b are the adjustable constants), it was possible to mathematically evaluate the reaction kinetics of cathodes in different electrolytes by comparing the b values [47,48]. The b values of NHCABT/$LiNO_3$-CBE in both cathodic (b_c) and anodic (b_a) processes (0.575 and 0.573) were higher than that of conventional CBE (0.554 and 0.511) (Fig. 5f), demonstrating that the introduction of synergistic dual additives could effectively improve reaction kinetics of the cathode materials.

The assembled Li||NCM811 batteries with NHCABT/$LiNO_3$-CBE also demonstrated improved electrochemical kinetics, rate performance, and cycling stability. When the current rates increased from 1.0 to 10.0 C (Fig. 5g), the Li||NCM811 batteries with conventional CBE exhibited markedly decreased specific discharge capacities. Especially at 10.0 C, an ultralow discharge capacity of only 23.1 mAh g^{-1} was delivered, indicating inferior reaction kinetics of the batteries. In contrast, the Li||NCM811 batteries with NHCABT/$LiNO_3$-CBE delivered reversible discharge capacities of 186.8, 154.5, 136.8, 122.5, and 107.1 mAh g^{-1} at 1.0, 3.0, 5.0, 7.0, and 10.0 C, respectively. The excellent rate performance highlighted the superiority of NHCABT/$LiNO_3$-CBE in accelerating Li^+ transfer, which was further verified by lower voltage polarization at different current rates (Fig. S30). The long-term cycling stability of Li||NCM811 batteries was investigated at 1.0 C (Fig. 5h). The batteries with conventional CBE suffered from a continuous capacity degradation only after 15 cycles due to the instability of native SEI under a high operating voltage of 4.4 V (vs. Li/Li^+), and a low discharge capacity of 48.8 mAh g^{-1} was delivered after 1000 cycles. Through introducing NHCABT/$LiNO_3$ into CBE, the Li||NCM811 batteries showed significantly improved cycling stability and well-maintained Coulombic efficiency, delivering a considerable discharge capacity of 138.3 mAh g^{-1} after 1000 cycles, corresponding to a capacity retention of 73.4 %. The impressive cycling stability of Li||NCM811 batteries encouraged us to further explore the application prospect of NHCABT/$LiNO_3$-CBE in Li||NCM811 pouch batteries. As shown in Fig. S31, the Li||NCM811 pouch batteries based on NHCABT/$LiNO_3$-CBE exhibited competitive cycling performance with a considerable capacity retention of 83.0 % at 0.5C after 150 cycles. The assembled pouch batteries successfully illuminated a light-emitting diode (LED) array panel, proving the feasibility and practicality of NHCABT/$LiNO_3$-CBE. By the combination of theoretical calculations and experimental analyses, the high compatibility of NHCABT/$LiNO_3$-CBE with aggressive NCM811 cathodes was verified. The markedly higher level of highest occupied molecular orbital (HOMO) of the activated NHCABT indicated its huge potential to tailor the chemical compositions of cathode interfaces (Fig. S32). To verify this inference, XPS analyses were performed to investigate the surface compositions of cycled NCM811 cathodes (Fig. S33). When using NHCABT/$LiNO_3$-CBE, the NCM811 cathodes exhibited distinct LiF and B—F characteristic peaks, indicating that the activated NHCABT could efficiently regulate the CEI compositions of NCM811 cathodes. Notably, for the N 1s spectrum, four signal peaks were detected when using NHCABT/$LiNO_3$-CBE, assigned to Li_3N, C—N, $LiNO_2$, and $LiNO_3$ species. Among them, the Li_3N, $LiNO_2$, and $LiNO_3$ species originated from the decomposition of the $LiNO_3$ additive, while the C—N species were attributed to the decomposition of the N-heterocyclic carbene part of NHCABT. Consequently, it concludes that, in addition to $–BF_3$ receptors, the remaining part of NHCABT will also be decomposed and modulate interfacial chemical compositions during the cycling processes of batteries.

To further evaluate the practical reliability, the Li||LFP batteries with high-loading cathodes (~15.3 mg cm^{-2} or ~2.6 mAh cm^{-2}) were assembled and tested (Fig. 6a). When using conventional CBE, the high-loading Li||LFP batteries could cycle stably for only 30 cycles at 1.0 C, and then exhibited continual capacity attenuation and unstable Coulombic efficiency with significant fluctuations (Fig. 6a, c). After 240 cycles, a low specific discharge capacity of only 21.8 mAh g^{-1} and a large overpotential were delivered. When changing to NHCABT/$LiNO_3$-

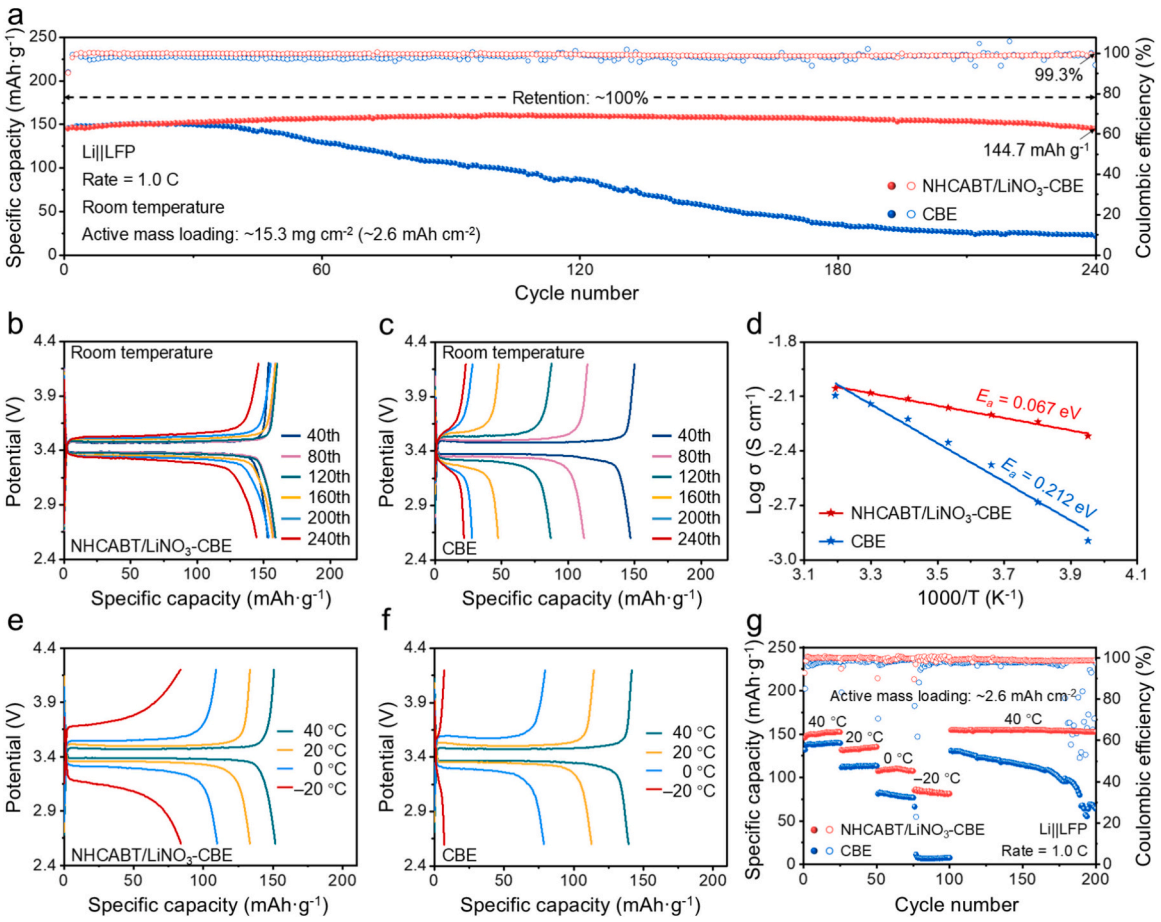

Fig. 6. Cycling stability and low-temperature electrochemical performances of high-loading Li||LFP batteries (~15.3 mg cm^{-2} or ~ 2.6 mAh cm^{-2}) based on NHCABT/$LiNO_3$-CBE and conventional CBE. (a) Room-temperature cycling performance of high-loading Li||LFP batteries measured at 1.0 C. (b, c) Galvanostatic charge/discharge profiles of different cycles for high-loading Li||LFP batteries based on (b) NHCABT/$LiNO_3$-CBE and (c) conventional CBE at room temperature. (d) Ionic conductivities of NHCABT/$LiNO_3$-CBE and conventional CBE as function of temperature ranging from +40 to −20 °C. (e, f) Galvanostatic charge/discharge profiles at different temperatures of high-loading Li||LFP batteries based on (e) NHCABT/$LiNO_3$-CBE and (f) conventional CBE. (g) Specific discharge capacities and Coulombic efficiencies at various temperatures from +40 to −20 °C of high-loading Li||LFP batteries measured at 1.0 C.

CBE, the high-loading Li||LFP batteries displayed exceptional cycling stability and limited voltage hysteresis (Fig. 6a, b). After 240 cycles, an ultrahigh specific discharge capacity of 144.7 mAh g^{-1} was still delivered, corresponding to an impressive capacity retention of almost 100 %. The prominent differences in cycling performance of high-loading Li||LFP batteries illustrated the great potential of synergistic dual electrolyte additives in boosting the durability of lithium metal batteries.

In consideration of the optimized Li^+ solvation structure and improved SEI compositions for NHCABT/$LiNO_3$-CBE, the low-temperature performance of NHCABT/$LiNO_3$-CBE was also investigated comprehensively. By carrying out EIS measurements of SS||SS symmetric batteries (Fig. S34), the temperature-dependent ionic conductivities of conventional CBE and NHCABT/$LiNO_3$-CBE were measured. The results showed that the ionic conductivity of conventional CBE sharply decreased from 8.00×10^{-3} S cm^{-1} to 1.27×10^{-3} S cm^{-1} with the drop of temperatures from +40 °C to −20 °C (Fig. S35). In contrast, the ionic conductivity of NHCABT/$LiNO_3$-CBE gently decreased from 8.79×10^{-3} S cm^{-1} to 4.81×10^{-3} S cm^{-1}. The outstanding ionic conductivity of NHCABT/$LiNO_3$-CBE was mainly attributed to its low Li^+ transport energy barrier. By fitting the linear relationship between the common logarithm of ionic conductivity and the temperatures, the apparent activation energy (E_a) for Li^+ transfer in different electrolytes was calculated (Fig. 6d) [49]. The NHCABT/$LiNO_3$-CBE displayed a much lower E_a of 0.067 eV than that of the CBE (0.212), confirming the advantages of synergistic dual additives in decreasing Li^+ transport energy barrier and facilitating rapid Li^+ transfer under low-temperature conditions. Based on the above theoretical calculations and systematic spectroscopic characterizations, we conclude that the improved low-temperature performance of NHCABT/$LiNO_3$-CBE is mainly attributed to two reasons: (1) the optimization of Li^+ solvation structure and (2) the formation of robust SEI with abundant inorganic species. The participation of NHCABT and NO_3^- in Li^+ solvation structure effectively weaken the interaction between Li^+ ions and solvent molecules in the electrolyte [35,50], thus enhancing the Li^+ desolvation capability [51], while the formation of stable SEI rich in Li_xN_y, Li_xNO_y, LiF and BF_x species effectively reduce the energy barrier for Li^+ diffusion, supporting rapid Li^+ migration through the SEI [52]. The cycling performances of high-loading Li||LFP batteries were further compared under different temperatures from +40 to −20 °C (Fig. 6e, f). Through galvanostatic charge/discharge at various temperatures, higher specific discharge capacities and lower voltage polarization were demonstrated when using NHCABT/$LiNO_3$-CBE, indicating the key role of the synergistic dual additives in enhancing low-temperature cycling stability.

The specific discharge capacities and Coulombic efficiencies of the high-loading Li||LFP batteries with conventional CBE or NHCABT/$LiNO_3$-CBE were systematically tested at different temperatures. As shown in Fig. 6g, the high-loading Li||LFP batteries with conventional CBE exhibited fast capacity reduction with the decrease of working temperatures from +40 to −20 °C. Especially, an ultralow discharge

capacity of only 6.8 mAh g^{-1} was presented at −20 °C. Even if the temperature recovered to +40 °C, continuous capacity degradation could still be observed, and finally the batteries failed. In comparison, the high-loading Li||LFP batteries with NHCABT/$LiNO_3$-CBE delivered stable discharge capacities of 151.1, 133.4, 109.3 and 82.8 mAh g^{-1} at the temperature of +40, +20, 0 and −20 °C, respectively. When the temperature was restored to +40 °C, the batteries could still cycle stably and deliver a well-recovered discharge capacity of 152.5 mAh g^{-1}. The above results demonstrate that the synergistic dual additives can enhance the low-temperature performance of batteries, making it possible for them to be widely applied in various regions and climates.

3. Conclusion

In summary, a well-designed synergistic-dual-additive electrolyte with optimized Li^+ solvation structure was developed by simultaneously introducing NHCABT and $LiNO_3$ into conventional carbonate-based electrolytes. A series of spectroscopic and electrochemical characterizations demonstrated that the addition of NHCABT with electron-deficient atoms could effectively increase the solubility of $LiNO_3$ from 0.08 wt% (0.0145 M) to 1.0 wt% (0.181 M). The dissolved NO_3^- could in turn activate the $–BF_3$ receptors of NHCABT, endowing it with high reactivity to participate in the formation of SEI. Benefiting from the synergistic effect of NHCABT and $LiNO_3$, Li^+ solvation chemistry was fully optimized, the compatibility of NHCABT/$LiNO_3$-CBE with lithium metal anodes was markedly enhanced, and a stable and ion-conducting artificial SEI was constructed. As a result, the Li||Li symmetric batteries based on NHCABT/$LiNO_3$-CBE achieved a stable Li plating/stripping process for over 1000 h. The Li||LFP batteries demonstrated an ultralong cycling lifespan of more than 3000 cycles at 2.0 C when using NHCABT/$LiNO_3$-CBE. The high-loading Li||LFP batteries (~15.3 mg cm^{-2} or ~2.6 mAh cm^{-2}) with NHCABT/$LiNO_3$-CBE could cycle stably for over 240 cycles with minimal capacity decay, and exhibited significantly improved low-temperature cycling stability at −20 °C. When using high-voltage NCM811 cathodes, the assembled Li||NCM811 batteries also perform well, presenting a highly reversible charge/discharge process for over 1000 cycles at 1.0 C. This work presents an intriguing synergistic dual-additive strategy and provides many meaningful insights for developing advanced electrolyte systems toward high-performance practical lithium metal batteries.

CRediT authorship contribution statement

Yaoda Wang: Writing – original draft, Methodology, Investigation, Formal analysis, Data curation, Conceptualization. **Junchuan Liang:** Methodology, Investigation, Data curation. **Xinmei Song:** Validation, Software, Methodology, Investigation. **Tianyu Shen:** Software, Methodology, Formal analysis. **Xingkai Ma:** Supervision, Methodology, Formal analysis, Data curation. **Zuoxiu Tie:** Validation, Software, Project administration, Investigation. **Zhong Jin:** Writing – review & editing, Supervision, Resources, Funding acquisition, Conceptualization.

Declaration of competing interest

The authors declare that they have no known competing financial interests or personal relationships that could have appeared to influence the work reported in this paper.

Acknowledgements

The authors appreciate the financial support from the National Natural Science Foundation of China (22479074 and 22475096), the Equipment Pre-Research and Ministry of Education Joint Fund General Project (8091B02052407), the Natural Science Foundation of Jiangsu Province (BK20240400 and BK20241236), the Science and Technology Major Project of Jiangsu Province (BG2024013), the Scientific and Technological Achievements Transformation Special Fund of Jiangsu Province (BA2023037), the Academic Degree and Postgraduate Education Reform Project of Jiangsu Province (JGKT24_C001), the Key Core Technology Open Competition Project of Suzhou City (SYG2024122), the Gusu Leading Talent Program of Scientific and Technological Innovation and Entrepreneurship of Wujiang District in Suzhou City (ZXL2021273), the open research fund of Suzhou Laboratory (SZLAB-1308-2024-TS005), and the Chenzhou National Sustainable Development Agenda Innovation Demonstration Zone Provincial Special Project (2023sfq11).

Appendix A. Supplementary data

Supplementary data to this article can be found online at https://doi.org/10.1016/j.cej.2025.166397.

Data availability

Data will be made available on request.

References

[1] M. Winter, B. Barnett, K. Xu, Before Li ion batteries, Chem. Rev. 118 (23) (2018) 11433–11456, https://doi.org/10.1021/acs.chemrev.8b00422.
[2] M. Li, J. Lu, Z.W. Chen, K. Amine, 30 years of lithium-ion batteries, Adv. Mater. 30 (33) (2018) 1800561, https://doi.org/10.1002/adma.201800561.
[3] J.M. Tarascon, M. Armand, Issues and challenges facing rechargeable lithium batteries, Nature 414 (2001) 359–367, https://doi.org/10.1038/35104644.
[4] B. Dunn, H. Kamath, J.M. Tarascon, Electrical energy storage for the grid: a battery of choices, Science 334 (6058) (2011) 928–935, https://doi.org/10.1126/science.1212741.
[5] X.B. Cheng, R. Zhang, C.Z. Zhao, Q. Zhang, Toward safe lithium metal anode in rechargeable batteries: a review, Chem. Rev. 117 (15) (2017) 10403–10473, https://doi.org/10.1021/acs.chemrev.7b00115.
[6] W. Xu, J.L. Wang, F. Ding, X.L. Chen, E. Nasybutin, Y.H. Zhang, J.G. Zhang, Lithium metal anodes for rechargeable batteries, Energy Environ. Sci. 7 (2) (2014) 513–537, https://doi.org/10.1039/C3EE40795K.
[7] D.C. Lin, Y.Y. Liu, Y. Cui, Reviving the lithium metal anode for high-energy batteries, Nat. Nanotechnol. 12 (2017) 194–206, https://doi.org/10.1038/nnano.2017.16.
[8] S.R. Chen, F. Dai, M. Cai, Opportunities and challenges of high-energy Lithium metal batteries for electric vehicle applications, ACS Energy Lett. 5 (10) (2020) 3140–3151, https://doi.org/10.1021/acsenergylett.0c01545.
[9] Q. Zhao, S. Stalin, L.A. Archer, Stabilizing metal battery anodes through the design of solid electrolyte interphases, Joule 5 (5) (2021) 1119–1142, https://doi.org/10.1016/j.joule.2021.03.024.
[10] C.J. Niu, H.L. Pan, J. Xiao, J.G. Zhang, L.L. Luo, C.M. Wang, D.H. Mei, J.S. Meng, X. P. Wang, Z.A. Liu, L.Q. Mai, J. Liu, Self-smoothing anode for achieving high-energy lithium metal batteries under realistic conditions, Nat. Nanotechnol. 14 (2019) 594–601, https://doi.org/10.1038/s41565-019-0427-9.
[11] M.D. Tikekar, S. Choudhury, Z.Y. Tu, L.A. Archer, Design principles for electrolytes and interfaces for stable lithium-metal batteries, Nat. Energy 1 (2016) 16114, https://doi.org/10.1038/nenergy.2016.114.
[12] S.F. Liu, J. Xiao Ji, S.Y. Yue, P.F. Hou, C.Y. Wang, J. Cui, B.W. Chen, J.R. Shao, F. D. Li, J.P. Tu Han, C.S. Wang, High interfacial-energy interphase promoting safe lithium metal batteries, J. Am. Chem. Soc. 142 (5) (2020) 2438–2447, https://doi.org/10.1021/jacs.9b11750.
[13] P. Bai, J. Li, F.R. Brushett, M.Z. Bazant, Transition of lithium growth mechanisms in liquid electrolytes, Energy Environ. Sci. 9 (10) (2016) 3221–3229, https://doi.org/10.1039/c6ee01674j.
[14] R. Bhattacharyya, B. Key, H. Chen, A.S. Best, A.F. Hollenkamp, C.P. Grey, In situ NMR observation of the formation of metallic lithium microstructures in lithium batteries, Nat. Mater. 9 (2010) 504–510, https://doi.org/10.1038/nmat2764.
[15] J.X. Zheng, M.S. Kim, Z.Y. Tu, S. Choudhury, T. Tang, L.A. Archer, Regulating electrodeposition morphology of lithium: towards commercially relevant secondary Li metal batteries, Chem. Soc. Rev. 49 (9) (2020) 2701–2750, https://doi.org/10.1039/C9CS00883G.
[16] Y.H. Tan, G.X. Lu, J.H. Zheng, F. Zhou, M. Chen, T. Ma, L.L. Lu, Y.H. Song, Y. Guan, J.X. Wang, Z. Liang, W.S. Xu, Y.G. Zhang, X.Y. Tao, H.B. Yao, Lithium fluoride in electrolyte for stable and safe lithium-metal batteries, Adv. Mater. 33 (42) (2021) 2102134, https://doi.org/10.1002/adma.202102134.
[17] S.Y. Li, L. Fan, Y.Y. Lu, Rational design of robust-flexible protective layer for safe lithium metal battery, Energy Storage Mater. 18 (2019) 205–212, https://doi.org/10.1016/j.ensm.2018.09.015.
[18] A.J. Hu, W. Chen, X.C. Du, Y. Hu, T.Y. Lei, H.B. Wang, L.X. Xue, Y.Y. Li, H. Sun, Y. C. Yan, J.P. Long, C.Z. Shu, J. Zhu, B.H. Li, X.F. Wang, J. Xiong, An artificial hybrid interphase for an ultrahigh-rate and practical lithium metal anode, Energy Environ. Sci. 14 (7) (2021) 4115–4124, https://doi.org/10.1039/D1EE00508A.

[19] Z.A. Yu, Y. Cui, Z.N. Bao, Design principles of artificial solid electrolyte interphases for lithium-metal anodes, Cell Rep. Phys. Sci. 1 (7) (2020) 100119, https://doi.org/10.1016/j.xcrp.2020.100119.
[20] X.L. Fan, L. Chen, X. Ji, T. Deng, S. Hou, J. Chen, J. Zheng, F. Wang, J.J. Jiang, K. Xu, C.S. Wang, Highly fluorinated interphases enable high-voltage Li-metal batteries, Chem 4 (1) (2018) 174–185, https://doi.org/10.1016/j.chempr.2017.10.017.
[21] X.Y. Zheng, L.Q. Huang, W. Luo, H.T. Wang, Y.M. Dai, X.Y. Liu, Z.Q. Wang, H. H. Zheng, Y.H. Huang, Tailoring electrolyte solvation chemistry toward an inorganic-rich solid-electrolyte interphase at a Li metal anode, ACS Energy Lett. 6 (6) (2021) 2054–2063, https://doi.org/10.1021/acsenergylett.1c00647.
[22] H.D. Yuan, J.W. Nai, H. Tian, Z.J. Ju, W.K. Zhang, Y.J. Liu, X.Y. Tao, X.W.(D.) Lou, An ultrastable lithium metal anode enabled by designed metal fluoride spansules, Sci. Adv. 6 (10) (2020) eaaz3112, https://doi.org/10.1126/sciadv.aaz3112.
[23] Y. Gao, T. Rojas, K. Wang, S. Liu, D.W. Wang, T.H. Chen, H.Y. Wang, A.T. Ngo, D. H. Wang, Low-temperature and high-rate-charging lithium metal batteries enabled by an electrochemically active monolayer-regulated interface, Nat. Energy 5 (2020) 534–542, https://doi.org/10.1038/s41560-020-0640-7.
[24] Y.J. Liu, X.Y. Tao, Y. Wang, C. Jiang, C. Ma, O.W. Sheng, G.X. Lu, X.W.(D.) Lou, Self-assembled monolayers direct a LiF-rich interphase toward long-life lithium metal anode, Science 375 (6582) (2022) 739–745, https://doi.org/10.1126/science.abn1818.
[25] J.Y. Wan, J. Xie, X. Kong, Z. Liu, K. Liu, F.F. Shi, A. Pei, H. Chen, W. Chen, J. Chen, X.K. Zhang, L.Q. Zong, J.Y. Wang, L.-Q. Chen, J. Qin, Y. Cui, Ultrathin, flexible, solid polymer composite electrolyte enabled with aligned nanoporous host for lithium batteries, Nat. Nanotechnol. 14 (2019) 705–711, https://doi.org/10.1038/s41565-019-0465-3.
[26] J.Y. Liang, X.X. Zeng, X.D. Zhang, T.T. Zuo, M. Yan, Y.X. Yin, J.L. Shi, X.W. Wu, Y. G. Guo, L.J. Wan, Engineering Janus interfaces of ceramic electrolyte via distinct functional polymers for stable high-voltage Li-metal batteries, J. Am. Chem. Soc. 141 (23) (2019) 9165–9169, https://doi.org/10.1021/jacs.9b03517.
[27] Q. Pang, X. Liang, I.R. Kochetkov, P. Hartmann, L.F. Nazar, Stabilizing lithium plating by a biphasic surface layer formed in situ, Angew. Chem. Int. Ed. 57 (31) (2018) 9795–9798, https://doi.org/10.1002/anie.201805456.
[28] S.P. Li, S. Fang, H. Dou, X.G. Zhang, Rbf as a dendrite-inhibiting additive in lithium metal batteries, ACS Appl. Mater. Interfaces 11 (23) (2019) 20804–20811, https://doi.org/10.1021/acsami.9b03940.
[29] C. Yan, Y.X. Yao, X. Chen, X.B. Cheng, X.Q. Zhang, J.Q. Huang, Q. Zhang, Lithium nitrate solvation chemistry in carbonate electrolyte sustains high-voltage lithium metal batteries, Angew. Chem. Int. Ed. 57 (43) (2018) 14055–14059, https://doi.org/10.1002/anie.201807034.
[30] Y.L. Jie, X.J. Liu, Z.W. Lei, S.Y. Wang, Y.W. Chen, F.Y. Huang, R.G. Cao, G. Q. Zhang, S.H. Jiao, Enabling high-voltage lithium metal batteries by manipulating solvation structure in ester electrolyte, Angew. Chem. Int. Ed. 59 (9) (2020) 3505–3510, https://doi.org/10.1002/anie.201914250.
[31] C.K. Fu, Y.L. Ma, S.F. Lou, C. Cui, L.Z. Xiang, W. Zhao, P.J. Zuo, J.J. Wang, Y. Z. Gao, G.P. Yin, A dual-salt coupled fluoroethylene carbonate succinonitrile-based electrolyte enables Li-metal batteries, J. Mater. Chem. A 8 (4) (2020) 2066–2073, https://doi.org/10.1039/c9ta11341j.
[32] H. Zheng, H.F. Xiang, F.Y. Jiang, Y.C. Liu, Y. Sun, X. Liang, Y.Z. Feng, Y. Yu, Lithium difluorophosphate-based dual-salt low concentration electrolytes for lithium metal batteries, Adv. Energy Mater. 10 (30) (2020) 2001440, https://doi.org/10.1002/aenm.202001440.
[33] H.L. Dai, K. Xi, X. Liu, C. Lai, S.Q. Zhang, Cationic surfactant-based electrolyte additives for uniform lithium deposition via lithiophobic repulsion mechanisms, J. Am. Chem. Soc. 140 (50) (2018) 17515–17521, https://doi.org/10.1021/jacs.8b08963.
[34] W.D. Zhang, Q. Wu, J.X. Huang, L. Fan, Z.Y. Shen, Y. He, Q. Feng, G.N. Zhu, Y. Y. Lu, Colossal granular lithium deposits enabled by the grain-coarsening effect for high-efficiency lithium metal full batteries, Adv. Mater. 32 (24) (2020) 2001740, https://doi.org/10.1002/adma.202001740.
[35] Z.H. Piao, P.T. Xiao, R.P. Luo, J.B. Ma, R.H. Gao, C. Li, J.Y. Tan, K. Yu, G.M. Zhou, H.M. Cheng, Constructing a stable Interface layer by tailoring solvation chemistry in carbonate electrolytes for high-performance lithium-metal batteries, Adv. Mater. 34 (8) (2022) 2108400, https://doi.org/10.1002/adma.202108400.
[36] S.Y. Li, W.D. Zhang, Q. Wu, L. Fan, X.Y. Wang, X. Wang, Z.Y. Shen, Y. He, Y.Y. Lu, Synergistic dual-additives electrolyte enables practical lithium metal batteries, Angew. Chem. Int. Ed. 59 (35) (2020) 14935–14941, https://doi.org/10.1002/anie.202004853.
[37] Z.X. Wang, F.L. Qi, L.C. Yin, Y. Shi, C.G. Sun, B.G. An, H.M. Cheng, F. Li, An anion-tuned solid electrolyte interphase with fast ion transfer kinetics for stable lithium anodes, Adv. Energy Mater. 10 (14) (2020) 1903843, https://doi.org/10.1002/aenm.201903843.
[38] T. Chen, W.H. Kong, P.Y. Zhao, H.N. Lin, Y. Hu, R.P. Chen, W. Yan, Z. Jin, Dendrite-free and stable lithium metal anodes enabled by an antimony-based lithiophilic interphase, Chem. Mater. 31 (18) (2019) 7565–7573, https://doi.org/10.1021/acs.chemmater.9b02356.
[39] H.N. Lin, Z.W. Zhang, Y.D. Wang, X.L. Zhang, Z.X. Tie, Z. Jin, Template-sacrificed hot fusion construction and nanoseed modification of 3D porous copper nanoscaffold host for stable-cycling lithium metal anodes, Adv. Funct. Mater. 31 (30) (2021) 2102735, https://doi.org/10.1002/adfm.202102735.
[40] Y.D. Wang, S.-W. Ke, G.F. Qiao, J.C. Liang, X.C. Zhou, X.M. Song, Z.X. Tie, S. Yuan, J.-L. Zuo, Z. Jin, Self-assembled lithiophilic interface with abundant nickel-Bis (Dithiolene) sites enabling highly durable and dendrite-free lithium metal batteries, Adv. Energy Mater. 14 (1) (2023) 2303051, https://doi.org/10.1002/aenm.202303051.
[41] X.S. Wang, S.W. Wang, H.R. Wang, W.Q. Tu, Y. Zhao, S. Li, Q. Liu, J.R. Wu, Y.Z. Fu, C.P. Han, Hybrid electrolyte with dual-anion-aggregated solvation sheath for stabilizing high-voltage lithium-metal batteries, Adv. Mater. 33 (2021) 2007945, https://doi.org/10.1002/adma.202007945.
[42] Z. Wang, Y. Wang, C. Wu, W.K. Pang, J. Mao, Z. Guo, Constructing Nitrided interfaces for stabilizing Li metal electrodes in liquid electrolytes, Chem. Sci. 12 (2021) 8945–8966, https://doi.org/10.1039/d1sc01806j.
[43] J. Pokharel, A. Cresce, B. Pant, M.Y. Yang, A. Gurung, W. He, A. Baniya, B. S. Lamsal, Z. Yang, S. Gent, X. Xian, Y. Cao, W.A. Goddard III, K. Xu, Y. Zhou, Manipulating the diffusion energy barrier at the lithium metal electrolyte interface for dendrite-free long-life batteries, Nat. Commun. 15 (2024) 3085, https://doi.org/10.1038/s41467-024-47521-z.
[44] X.Y. Ma, J.T. Yu, X.Y. Zou, Y. Hu, M.C. Yang, F. Zhang, F. Yan, Single additive to regulate lithium-ion solvation structure in carbonate electrolytes for high-performance lithium-metal batteries, Cell Rep. Phys. Sci. 4 (2023) 101379, https://doi.org/10.1016/j.xcrp.2023.101379.
[45] J.H. Zhou, X.Y. Lian, Q.T. Shi, Y. Liu, X.Q. Yang, A. Bachmatiuk, L.J. Liu, J.Y. Sun, R.Z. Yang, J.-H. Choi, M.H. Rummeli, Dual-salt electrolyte additives enabled stable lithium metal anode/lithium–manganese-rich cathode batteries, Adv. Energy Sustain. Res. 3 (1) (2022) 2100140, https://doi.org/10.1002/aesr.202100140.
[46] B.D. Adams, J.M. Zheng, X.D. Ren, W. Xu, J.-G. Zhang, Accurate determination of coulombic efficiency for lithium metal anodes and lithium metal batteries, Adv. Energy Mater. 8 (7) (2018) 1702097, https://doi.org/10.1002/aenm.201702097.
[47] V. Augustyn, J. Come, M.A. Lowe, J.W. Kim, P.-L. Taberna, S.H. Tolbert, H. D. Abruña, P. Simon, B. Dunn, High-rate electrochemical energy storage through Li^+ intercalation pseudocapacitance, Nat. Mater. 12 (2013) 518–522, https://doi.org/10.1038/nmat3601.
[48] Z. Li, J.T. Zhang, Y. Lu, X.W. Lou, A Pyrolyzed polyacrylonitrile/selenium disulfide composite cathode with remarkable lithium and sodium storage performances, Sci. Adv. 4 (6) (2018) eaat1687, https://doi.org/10.1126/sciadv.aat1687.
[49] L.F. Tang, B.W. Chen, Z.H. Zhang, C.Q. Ma, J.C. Chen, Y.G. Huang, F.R. Zhang, Q. Y. Dong, G.Y. Xue, D.Q. Chen, C.J. Hu, S.Z. Li, Z. Liu, Y.B. Shen, Q. Chen, L. W. Chen, Polyfluorinated crosslinker-based solid polymer electrolytes for long-cycling 4.5 V lithium metal batteries, Nat. Commun. 14 (2023) 2301, https://doi.org/10.1038/s41467-023-37997-6.
[50] F. Huang, Y. Zhong, M. Qin, J. Qiu, C. Hu, P. Xu, H. Zhang, C. Sheng, S. Liang, G. Fang, Weakly anion-driven solvation towards stable operation of carbonate ester-based sodium metal batteries at −40 °C, Chem. Eng. J. 511 (2025) 162150, https://doi.org/10.1016/j.cej.2025.162150.
[51] F. Zhu, J. Wang, Y. Zhang, H. Tu, X. Xia, J. Zhang, H. He, H. Lin, M. Liu, Low-temperature lithium metal batteries achieved by synergistically enhanced screening Li^+ desolvation kinetics, Adv. Mater. 37 (2025) 2411601, https://doi.org/10.1002/adma.202411601.
[52] C. Thenuwara, P.P. Shetty, N. Kondekar, S.E. Sandoval, K. Cavallaro, R. May, C. T. Yang, L.E. Marbella, Y. Qi, M.T. McDowell, Efficient low-temperature cycling of lithium metal anodes by tailoring the solid-electrolyte interphase, ACS Energy Lett. 5 (2020) 2411–2420, https://doi.org/10.1021/acsenergylett.0c01209.